STU
FCHPT

Graphitic carbon nitride/activated carbon composite inks for screen-printed electrodes: Influence of composition on rheology, microstructure and electrochemical performance

Pavol Gemeiner[1], Michal Hatala[1], Katarína Gregová[1], Lukáš Gál[1], Katarína Tomanová[2], Ľubomír Švorc[3]

[1]*Department of Graphic Arts Technology and Applied Photochemistry, Faculty of Chemical and Food Technology, Slovak University of Technology in Bratislava, Radlinského 9, 812 37 Bratislava, Slovakia*
[2]*Department of Plastics, Rubber and Fibres, Faculty of Chemical and Food Technology, Slovak University of Technology in Bratislava, Radlinského 9, 812 37 Bratislava, Slovakia*
[3]*Institute of Analytical Chemistry, Faculty of Chemical and Food Technology, Slovak University of Technology in Bratislava, Radlinského 9, 812 37 Bratislava, Slovakia*
pavol.gemeiner@stuba.sk

Abstract: Composition of conductive inks plays a decisive role in determining both printability and electrochemical performance of screen-printed electrochemical sensors. In this work, composite conductive inks based on graphitic carbon nitride (g-C_3N_4) and activated carbon (AC) were prepared with systematically varied filler ratios and evaluated by rheological measurements, scanning electron microscopy, cyclic voltammetry, and electrochemical impedance spectroscopy. All inks exhibited shear-thinning behavior suitable for screen printing, while increasing the g-C_3N_4 content enhanced the low-shear viscosity and promoted rapid structural recovery after shear. Scanning electron microscopy revealed that nanosized g-C_3N_4 filled the interparticle voids between larger AC particles, producing a denser and more homogeneous composite microstructure. Electrochemical performance was evaluated using a $[Fe(CN)_6]^{3-/4-}$ redox probe. Increasing the AC fraction reduced the peak-to-peak separation from 130 mV for pure g-C_3N_4 electrode to 100 mV for the 50:50 and 25:75 composites, indicating more facile interfacial charge-transfer kinetics, although the associated Faradaic peak currents decreased with the increasing AC content due to lower density of g-C_3N_4-associated redox-active sites. Electrochemical impedance spectroscopy showed a substantial decrease in charge-transfer resistance from 148.5 $\Omega \cdot cm^2$ for pure g-C_3N_4 to 7.2 $\Omega \cdot cm^2$ for g-C_3N_4:AC (25:75) composite, outperforming even pure AC electrode (16.9 $\Omega \cdot cm^2$). The results demonstrate synergistic interaction between both conductive components. Both materials, g-C_3N_4 and AC, provide electrochemically active surface sites that promote the Faradaic response, whereas AC establishes an efficient conductive network that facilitates charge transport. The optimized g-C_3N_4:AC (25:75) represents a promising conductive ink for the fabrication of low-cost, reliable, screen-printed electrodes that can be readily modified through further surface or bulk functionalization for diverse electrochemical sensing applications.

Keywords: activated carbon; conductive inks; electrochemical sensors; graphitic carbon nitride; screen-printed electrodes

Introduction

Printed electrochemical sensors have become one of the most rapidly developing analytical platforms owing to their low manufacturing cost, portability, rapid response, and suitability for large-scale production. Among the available fabrication techniques, screen printing has attracted particular attention because it enables reproducible fabrication of disposable electrochemical devices with high production throughput while maintaining excellent analytical performance (Orzari et al., 2025). Analytical performance of screen-printed electrodes depends not only on electrode design but also on the composition of the conductive ink. Conductive inks are multicomponent systems consisting of conductive fillers, polymeric binders, solvents, and functional additives, whose mutual interactions determine printability, adhesion to the substrate, mechanical stability, and electrical conductivity of the printed electrode (Hatala et al., 2019). Besides electrical conductivity, rheological properties of conductive inks play a decisive role during screen printing (Budny et al., 2022). Appropriate viscosity and pronounced shear-thinning behavior ensure efficient ink transfer through the printing mesh, homogeneous layer formation, and rapid structural recovery after deposition, whereas unsuitable rheological properties may result in poor print definition, inhomogeneous conductive pathways, and reduced electrochemical performance (Hatala et al., 2019).

Carbon-based materials remain the most widely used conductive fillers for printable electrochemical electrodes because they combine high electrical conductivity, broad electrochemical potential windows, chemical stability, and relatively low production costs (Gibi et al., 2024). Depending on the intended application, graphite, carbon black, graphene, carbon nanotubes, and activated carbon can be used either individually or in composite formulations to tailor the electrochemical behavior of printed electrodes (Crapnell and Banks, 2024). Among emerging carbon-based functional materials, graphitic carbon nitride (g-C_3N_4) has attracted considerable attention because of its two-dimensional conjugated structure, high nitrogen content, chemical stability, and abundance of catalytically active surface sites. These structural characteristics facilitate adsorption of electroactive species and promote interfacial electron-transfer processes, making g-C_3N_4 an attractive material for electrochemical sensing applications (Puentes-Prado et al., 2022; de Faria et al., 2024). Despite these attractive properties, practical application of pristine g-C_3N_4 in electrochemical sensors is restricted by its relatively low intrinsic electrical conductivity. Consequently, numerous studies have combined g-C_3N_4 with conductive carbon materials, metal oxides, or conductive polymers to improve charge-transfer kinetics and enhance the analytical performance of electrochemical sensors (Wang et al., 2022). Activated carbon is another attractive carbon material for electrochemical applications because it combines high specific surface area, hierarchical porosity, good electrical conductivity, and excellent chemical stability. These characteristics increase the electrochemically active surface area, facilitate mass transport, and improve electron-transfer processes, making activated carbon an effective conductive component for electrochemical sensors and printed electrodes (Gissawong et al., 2021). Recent studies have demonstrated that activated carbon can be successfully incorporated into screen-printed electrodes, where it enhances analytical sensitivity and lowers detection limits through the formation of an efficient conductive network and increased accessibility of electroactive sites (Santos et al., 2025).

Most reported g-C_3N_4-based electrochemical sensors rely on surface modification of previously fabricated electrodes by drop-casting or deposition of nanocomposites containing g-C_3N_4. Such an approach effectively improves the electrode/electrolyte interface but does not address the influence of g-C_3N_4 on the bulk properties of printable conductive materials or on the printing process itself (Singh et al., 2024). More recently, g-C_3N_4 has also been incorporated into alternative printed electrode platforms, including conductive polymer composites for additive manufacturing and conductive paste electrodes, demonstrating that bulk incorporation of this material can improve electrochemical performance while preserving the simplicity of electrode fabrication (Mutic et al., 2024). Despite these advances, studies systematically investigate conductive inks in which graphitic carbon nitride constitutes an integral component of the conductive phase together with activated carbon remain scarce. In particular, the relationships between filler composition, rheological behavior, structural organization of the printed layer, and electrochemical performance have not yet been comprehensively established.

Therefore, the present work focuses on the preparation of conductive composite inks containing graphitic carbon nitride and activated carbon in systematically varied mass ratios, and on the evaluation of their rheological, structural, morphological, and electrochemical properties. Unlike conventional approaches based on post-fabrication surface modification, graphitic carbon nitride is incorporated directly into the conductive printing ink, allowing the influence of the conductive phase composition on both printing behavior and electrode performance to be investigated. This study provides a comprehensive understanding of the role of g-C_3N_4/activated carbon composition in the design of printable conductive materials for electrochemical sensing applications.

Materials and Methods

g-C_3N_4 synthesis

Graphitic carbon nitride (g-C_3N_4) was synthesized by thermal polycondensation of melamine (Sigma-Aldrich). Briefly, 10 g of melamine were placed into a covered ceramic crucible and heated in a muffle furnace at 550 °C for 4 h using a heating rate of 2 °C · min^{-1}. After natural cooling to room temperature, the obtained yellow product was ground into a fine powder and used without further purification.

Preparation of gCN:AC inks for screen-printing

Printing inks were prepared in batches of 4 g using a binder system consisting of 8 wt. % ethyl cellulose dissolved in diethylene glycol monobutyl ether. Exact compositions of the prepared inks are presented in Tab. 1. The inks were formulated using synthetized graphitic carbon nitride and commercially obtained activated carbon (C4386, Sigma-Aldrich: $S_{BET} \sim 1100$ $m^2 \cdot g^{-1}$; $Vp \sim 0.9$ $cm^3 \cdot g^{-1}$; D50 < 44 μm). Particle content was fixed at 20 wt. % for all samples, except for that based only on

gCN. As gCN:AC 100:0 exhibited excessively high viscosity, 20 wt. % DEGBE was added during the mixing process to reduce its viscosity and sustain its printability. The binder solution was prepared by dissolving the required amount of EC in DEGBE under continuous magnetic stirring at 60 °C for 3 h to ensure complete polymer dissolution. Following binder preparation, the particles were added to the corresponding amount of the binder and homogenized using a manual mixing device. To minimize excessive heating during processing, mixing was carried out in five consecutive intervals of 30 s each.

Preparation of screen-printed gCN:AC electrodes

gCN:AC electrodes with a size of 10 × 10 mm were prepared by screen printing (mesh PME 71-48 Y) inks onto fluorine-doped tin oxide (FTO)-coated glass substrates (15 × 20 mm, sheet resistance of 7 $\Omega \cdot sq^{-1}$; Sigma-Aldrich). Prior to printing, the FTO substrates were cleaned using a three-step ultrasonic cleaning procedure consisting of detergent solution, acetone, and isopropyl alcohol, followed by drying under ambient conditions.

Tab. 1. Composition of the prepared screen-printing gCN:AC inks.

gCN:AC	EC (g)	DEGBE (g)	gCN (g)	AC (g)
100:0	0.256	3.744	0.8	0
75:25	0.256	2.944	0.6	0.2
50:50	0.256	2.944	0.4	0.4
25:75	0.256	2.944	0.2	0.6
0:100	0.256	2.944	0	0.8

Methods

FTIR spectra of g-C_3N_4 powder were recorded using a Thermo Scientific Nicolet iS20 FTIR spectrometer equipped with a ZnSe attenuated total reflectance (ATR) crystal. The spectrum was acquired by averaging 32 scans to improve the signal-to-noise ratio. Spectra were collected over the 3600—600 cm^{-1} spectral range at a spectral resolution of 4 cm^{-1}. Raman spectra of the synthesized g-C_3N_4 powder were acquired using a DXR™ 3xi Raman Imaging Microscope (Thermo Scientific™, USA) with a 785 nm excitation laser. Rheological properties of the prepared gCN:AC inks were evaluated using a Haake Mars iQ Air rotational rheometer at a controlled temperature of 25 °C. All measurements were carried out using parallel plate geometry P20/Ti (20 mm diameter) with a gap setting of 0.2 mm. Before each measurement, the samples were subjected to a conditioning procedure consisting of equilibration at the shear rate of 0.1 s^{-1} for 120 s at 25 °C, followed by a resting period of 300 s at zero shear rate to allow relaxation of residual stresses. Flow and viscosity curves were obtained by measuring the dependence of shear stress on shear rate. A controlled shear rate sweep from 0.2 to 2000 s^{-1} was applied using logarithmic progression with 50 measurement points over a total test duration of 250 s. Viscosity recovery (thixotropy) was investigated using a three-step shear test. Following the conditioning and relaxation stages, samples were sheared at 0.1 s^{-1} for 180 s to establish the initial structural state. Shear rate of 2000 s^{-1} was then applied for 30 s to induce structural breakdown. Subsequently, viscosity recovery was monitored at the shear rate of 0.1 s^{-1} for 240 s. Surface morphology of the screen-printed electrodes was examined using a JEOL JSM-7500F scanning electron microscope (Japan) operated at accelerating voltages of 5 and 15 kV. Prior to imaging, the samples were sputter-coated with an Au-Pd alloy under Ar atmosphere using a BALZERS sputter coater. SEM micrographs were acquired digitally using the PC SEM software (version 3.0.1.8). Cyclic voltammetry (CV) and electrochemical impedance spectroscopy (EIS) measurements were performed using a PalmSens4 potentiostat/galvanostat (PalmSens BV, The Netherlands) controlled by the PSTrace software. Faradaic peak currents were determined using the PSTrace software's automatic peak-search function, which computes peak height relative to a locally interpolated baseline established from the regions flanking each peak. This procedure was also applied to all compositions. gCN:AC electrodes served as the working electrodes in a conventional three-electrode electrochemical cell, with a Pt plate as the counter electrode and an Ag/AgCl (3 M KCl) electrode as the reference electrode. Cyclic voltammograms were recorded over the potential range from −0.10 to 0.55 V at the scan rate of 100 $mV \cdot s^{-1}$. Electrochemical impedance spectroscopy measurements were carried out over the frequency range of 1 Hz to 10 kHz at the applied direct current potential of 0.20 V (vs. Ag/AgCl) using an alternating current perturbation amplitude of 10 mV. All electrochemical measurements were performed in 1 mM potassium ferricyanide ($K_3[Fe(CN)_6]$) with 0.1 M KCl as the supporting electrolyte. Electrochemical parameters (I_{pa}, I_{pc}, R_{ct}) reported in Tab. 2 represent the mean of n = 5 independently prepared electrodes per sample. The corresponding relative standard deviation (RSD, %) is reported alongside each value in Tab. 2.

Results and discussion

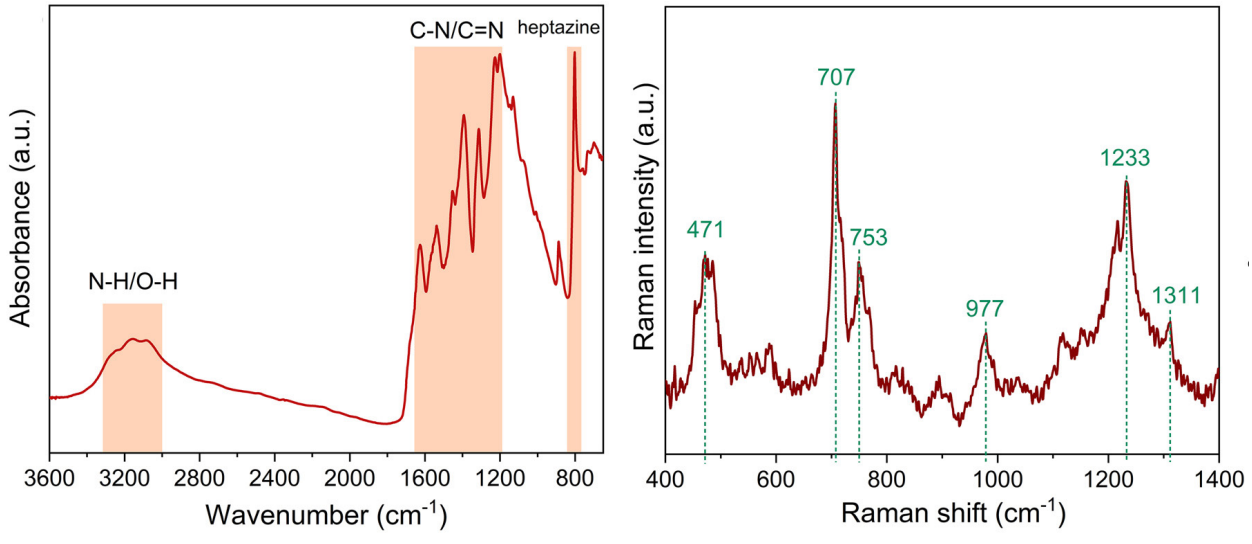
Fourier-transform infrared (FTIR) and Raman spectroscopy were employed to investigate chemical

structure of graphitic carbon nitride (g-C_3N_4) synthesized by thermal condensation of melamine. FTIR spectra (Fig. 1a) exhibit characteristic vibrational fingerprint of polymeric g-C_3N_4, confirming successful formation of the heptazine (tri-*s*-triazine)-based carbon nitride framework. The broad absorption region between 1200 and 1650 cm^{-1} is assigned to the stretching vibrations of aromatic C—N and C=N bonds, reflecting the formation of an extended conjugated heterocyclic network. The distinct absorption band at approximately 804 cm^{-1} corresponds to the breathing mode of heptazine (tri-*s*-triazine) units and is considered a characteristic signature of the graphitic carbon nitride structure. Furthermore, a broad band observed in the 3000–3300 cm^{-1} region is attributed to the stretching vibrations of terminal N—H groups and O—H groups originating from adsorbed water molecules, which is commonly observed for g-C_3N_4 materials (Zhang et al., 2022). The absence of additional absorption bands related to residual precursor species, such as C—H or carbonyl-containing groups, indicates efficient thermal condensation of melamine and high chemical purity of the prepared samples.

Raman spectra (Fig. 1b) further confirmed successful synthesis of polymeric g-C_3N_4 and were fully consistent with the FTIR results. Several characteristic Raman bands were observed at approximately 471, 753, 977, 1233, and 1311 cm^{-1}, which are attributed primarily to the stretching vibrations of C—N bonds within the aromatic heptazine framework and are in good agreement with previously reported Raman spectra of graphitic carbon nitride (Li et al., 2012). The complementary FTIR and Raman results consistently confirm successful formation of a well-condensed polymeric g-C_3N_4 structure with the characteristic heptazine-based framework.

The synthesized graphitic carbon nitride (g-C_3N_4, gCN) was mixed with activated carbon (AC) in different weight ratios (gCN:AC = 100:0, 75:25, 50:50, 25:75, and 0:100) to prepare screen-printable colloidal inks using ethyl cellulose as a polymeric rheological agent and binder. Rheological properties of printing inks are the key parameters determining their suitability for a particular printing technique. In the present work, the formulations were designed for screen printing which requires sufficiently high viscosity at rest combined with pronounced shear-thinning behavior under high shear conditions encountered during printing.

Viscosity curves and flow curves of the investigated inks are presented in Fig. 2a and Fig. 2b, respectively. All gCN:AC inks exhibited non-Newtonian pseudoplastic behavior characterized by continuous decrease in viscosity with increasing shear rate. Such shear-thinning behavior is advantageous for screen printing because the viscosity decreases during printing, facilitating the passage of the ink through the screen mesh while recovering after deposition to maintain the printed pattern (Gemeiner et al., 2013). Because of the substantially different morphology and surface characteristics of gCN and AC particles, it was not possible to identify a single measuring geometry that was equally suitable for all formulations. This limitation is particularly evident for AC-rich formulations (gCN:AC 0:100 and 25:75), which exhibited low viscosity together with only a slight decrease in viscosity with increasing shear rate. Consequently, rheological parameters

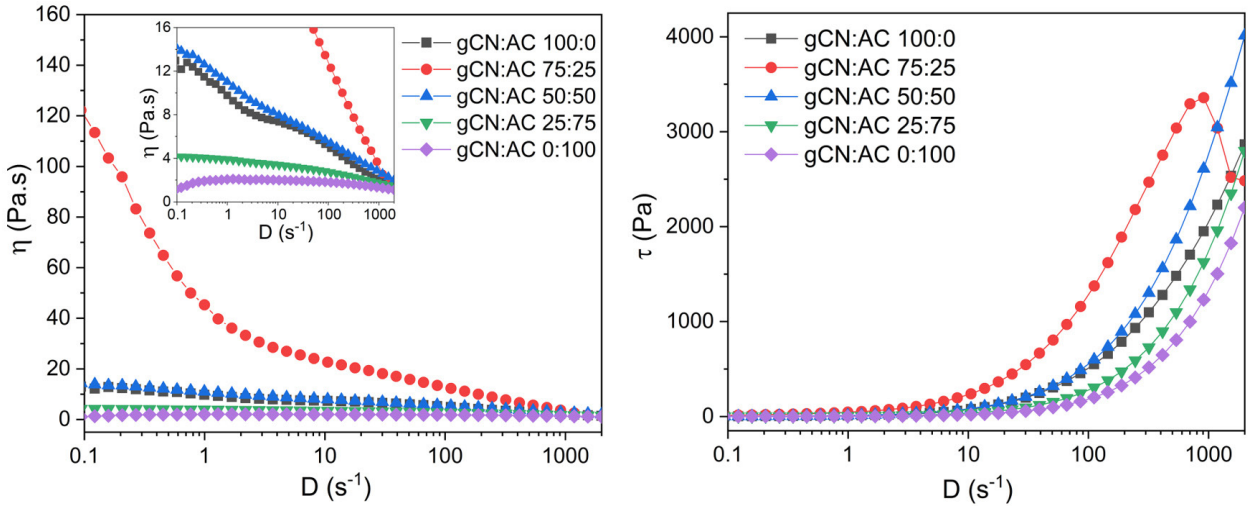


a) b)

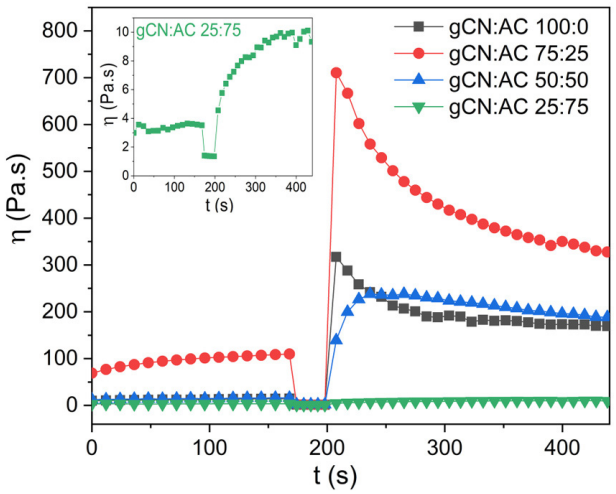
Fig. 1. FTIR (a) and Raman spectra (b) of g-C_3N_4 synthesized from melamine precursor.

obtained for these two formulations should be interpreted with caution. Viscosity curves further demonstrate that increasing the gCN content markedly increased the viscosity of the inks, particularly in the low-shear region. The highest viscosity was observed for the gCN:AC 75:25 formulation. Interestingly, the gCN:AC 100:0 ink, despite requiring additional dilution during formulation, still exhibited higher viscosity than the AC-rich inks (gCN:AC 0:100 and 25:75), confirming the dominant contribution of gCN particles to the rheological response of the dispersions.

Flow curves (Fig. 2b) reveal a continuous increase in shear stress with increasing shear rate for all formulations. At low shear rates (< 10 s^{-1}), only minor differences in shear stress were observed between the individual inks, whereas the differences became progressively more pronounced at higher shear rates (> 10 s^{-1}). The gCN:AC 75:25 formulation exhibited the highest shear stress over most of the investigated shear-rate range, reflecting the strongest resistance to flow. Interestingly, at shear rates of approximately 800 s^{-1}, this formulation showed a slight decrease in shear stress despite the increasing shear rate. Such behavior may indicate the disruption of a transient supramolecular particle network formed through interparticle interactions between particles and the ethyl cellulose binder. This behavior was observed only for the gCN:AC 75:25 formulation, which also exhibited the highest low-shear viscosity, indicating that this composition develops the strongest internal particle network among the investigated dispersions. Overall, these results further confirm that increasing the gCN content enhances the internal particle interactions, which leads to stronger structural network within the ink.



a) b)



c)

Fig. 2. Rheology measurements of gCN:AC inks: a) viscosity as a function of shear rate, b) shear stress as a function of shear rate, c) viscosity recovery test.

The viscosity recovery behavior is presented in Fig. 2c. Measurements were performed only for inks containing gCN because the viscosity of pure AC formulation was too low to provide reliable data under the selected experimental conditions. Unlike conventional thixotropic systems, which typically exhibit gradual monotonic recovery of viscosity following shear reduction, the investigated inks display non-standard recovery characterized by pronounced viscosity overshoot. Immediately after the high-shear interval, the viscosity rapidly increased to a maximum before gradually decreasing towards a quasi-equilibrium value. The magnitude of this transient overshoot increased systematically with increasing gCN content and was most pronounced for the gCN:AC 75:25 and gCN:AC 100:0 formulations. In contrast, the gCN:AC 25:75 ink exhibited only a negligible overshoot effect. This behavior suggests that gCN particles dominate the structural evolution of the dispersions during recovery. Exposure to high shear likely disrupts the particle network and promotes particle rearrangement. Immediately after the shear rate is reduced, a transient network with enhanced resistance to flow is rapidly rebuilt, producing the observed viscosity overshoot. As structural relaxation proceeds, this temporary network gradually reorganizes, resulting in a decrease in viscosity towards a new equilibrium state. Nevertheless, the initial viscosity measured before the high-shear interval was not completely recovered within the investigated time window. From the perspective of screen printing, this recovery behavior may have both beneficial and adverse consequences. The rapid viscosity increase immediately after deposition can suppress levelling of the printed layer, potentially increase surface roughness, and enhance replication of the screen mesh pattern. Conversely, rapid rebuilding of the internal structure improves dimensional stability of the deposited ink and reduces spreading of printed features. Consequently, formulations exhibiting a viscosity overshoot may be particularly advantageous for printing fine conductive patterns where accurate preservation of feature geometry is essential.

Fig. 3 presents optical and SEM images of the screen-printed gCN:AC electrodes. The optical image (Fig. 3, top) shows 1 × 1 cm electrodes printed on 1.5 × 2 cm FTO substrates. Pronounced differences in particle morphology, size, and surface texture were observed between pristine g-C_3N_4 and AC (Fig. 3a—f). Synthesized g-C_3N_4 consists of submicrometer particles with lateral dimensions ranging from several tens to several hundreds of nanometers. At higher magnification (30 000×, Fig. 3c), the material exhibits the characteristic layered morphology of stacked nanosheets with an estimated thickness of approximately 10—20 nm. Accordingly, the synthesized g-C_3N_4 possesses a relatively low specific surface area and pore volume (S_{BET} = 10 $m^2 \cdot g^{-1}$, V_p = 0.11 $cm^3 \cdot g^{-1}$), consistent with bulk g-C_3N_4 prepared by direct thermal polymerization of melamine without exfoliation or templating treatments (Alwin et al., 2020). In contrast, AC exhibited substantially higher specific surface area ($S_{BET} \approx 1100$ $m^2 \cdot g^{-1}$) and pore volume ($V_p \approx 0.90$ $cm^3 \cdot g^{-1}$). AC particles were considerably larger, reaching several tens of micrometers with a median particle size (D50) of approximately 20—40 μm (Fig. 3e, f). These differences in particle size strongly influenced the packing behavior and, consequently, the microstructure of printed electrodes. The electrode prepared solely from AC (Fig. 3d—f) exhibited a heterogeneous surface composed of loosely packed coarse particles, resulting in incomplete substrate coverage and local exposure of the FTO surface. In contrast, the pure g-C_3N_4 electrode (Fig. 3a—c) formed a compact and continuous coating because the fine nanosheets uniformly covered the substrate. However, microcracks were observed in all g-C_3N_4-containing electrodes. These cracks most likely originated from shrinkage stress generated during solvent evaporation and thermal treatment, a phenomenon commonly observed in nanoparticle-based thick films (Weldon et al., 2017). Their density and width gradually decreased with increasing AC content (Fig. 3g—i), suggesting that the coarse AC particles acted as a mechanically rigid framework that partially suppressed drying shrinkage and relieved internal stress. Despite the presence of these cracks, all printed layers exhibited excellent adhesion to the FTO substrate, and no delamination or mechanical peeling was observed. The composite electrodes (Fig. 3g—i) exhibited homogeneous distribution of AC particles throughout the printed layer. Owing to their much smaller size, the g-C_3N_4 nanoparticles occupied the interparticle voids between the larger AC particles, producing a denser and more uniform microstructure than that of the pure AC electrode. This matrix-forming role of g-C_3N_4 became particularly evident in g-C_3N_4-rich compositions, where the porous AC particles were uniformly embedded within the g-C_3N_4 framework while maintaining good spatial dispersion. Overall, SEM observations demonstrate that the g-C_3N_4 ratio governs the packing density, structural continuity, and surface homogeneity of screen-printed electrodes. The combination of nanosized g-C_3N_4 and micrometer-sized AC produces a hierarchical composite architecture in which g-C_3N_4 improves particle packing, whereas AC provides a porous conductive phase. As discussed in the following section, this optimized microstructure

facilitates electron transport while preserving electrolyte accessibility, ultimately leading to improved electrochemical performance.

Electrochemical behavior of screen-printed gCN:AC electrodes was investigated by cyclic voltammetry (CV) and electrochemical impedance spectroscopy (EIS), including Nyquist plots, Bode phase plots, and impedance magnitude analyses (Fig. 4). All measurements were performed in an aqueous electrolyte containing 1 mM $[Fe(CN)_6]^{3-/4-}$ and 0.1 M KCl. These complementary techniques provide information on the Faradaic activity, charge-transfer kinetics and electrical properties of printed composite electrodes.

Cyclic voltammograms (Fig. 4a) exhibited well-defined anodic and cathodic peaks for all gCN-containing electrodes, indicating quasi-reversible redox behavior. Increasing the AC content progressively enlarged the voltametric area, reflecting a greater capacitive contribution arising from the high specific surface area and porous structure of AC. Therefore, electrochemical parameters summarized in Tab. 2 were determined after subtraction of the capacitive background current to enable quantitative comparison of the Faradaic response. Pristine g-C_3N_4 electrodes exhibited the highest anodic and cathodic peak currents (129.1 µA and −120.3 µA, respectively). Increasing the AC fraction gradually reduced both peak currents, while the pure AC electrode displayed only a weak anodic peak together with a highly asymmetric cathodic response (I_{pa}/I_{pc} = −0.20). The decrease in I_p with

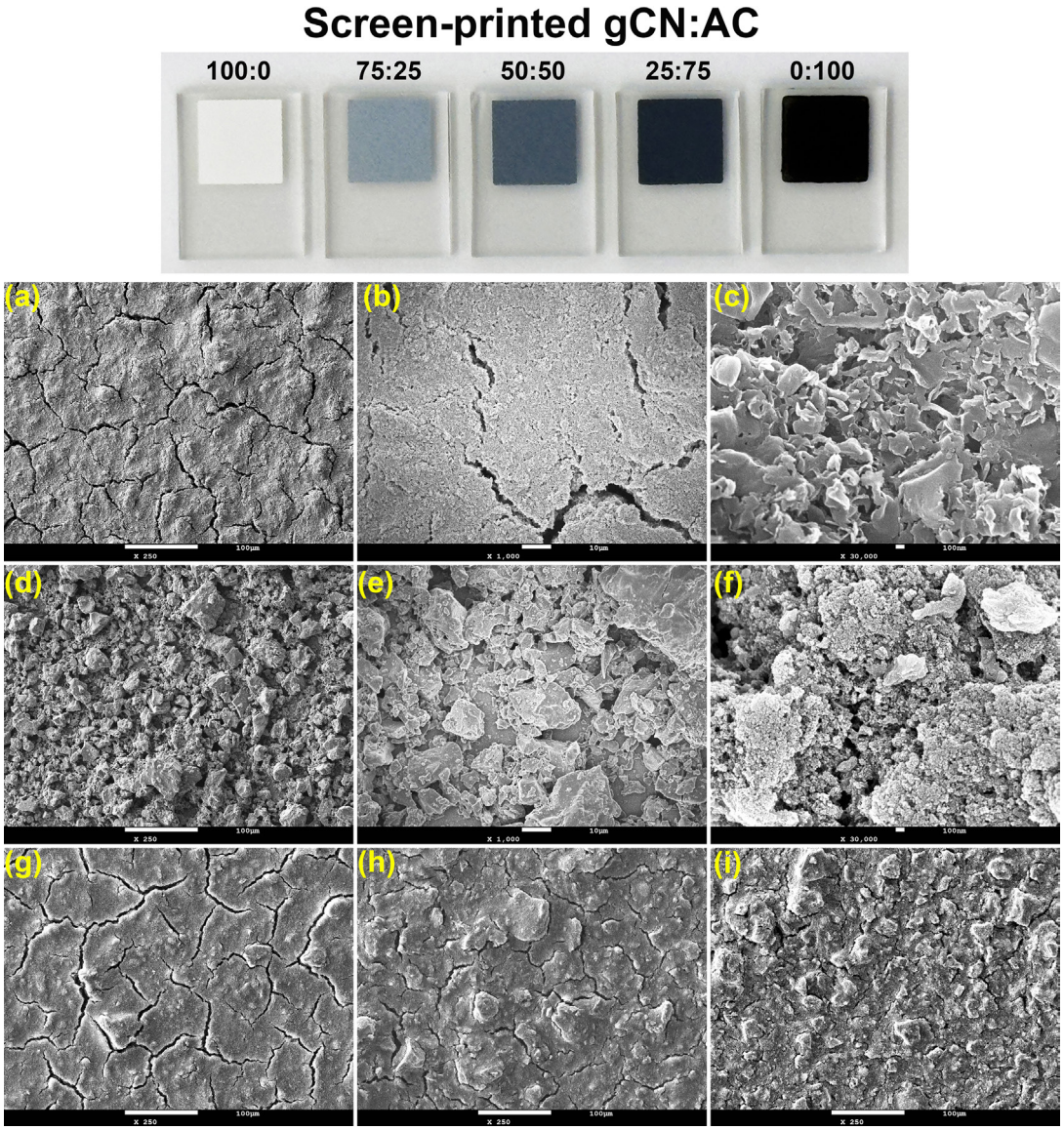


Fig. 3. Optical image of screen-printed gCN:AC electrodes on FTO substrates. SEM images of gCN:AC electrodes: (a, b, c) gCN:AC 100:0, (d, e, f) gCN:AC 0:100, (g) gCN:AC 75:25, (h) gCN:AC 50:50, (i) gCN:AC 25:75.

increasing AC content is attributed to a decrease in effective electroactive area; specifically, the density of gCN-associated sites capable of Faradaic exchange with $[Fe(CN)_6]^{3-/4-}$; rather than to the geometric electrode area which was held constant across compositions. These observations indicate that g-C_3N_4 provides electrochemically active sites responsible for the Faradaic processes, whereas AC mainly contributes to non-Faradaic charge storage through electric double-layer capacitance. Similar enhancement of Faradaic activity by g-C_3N_4-modified screen-printed electrodes has been reported previously (Jahani et al., 2022). At the same time, increasing the AC content reduced the peak-to-peak separation (ΔE_p) from 130 mV for pristine gCN to 100 mV for the 50:50 and 25:75 composites, indicating progressively faster electron-transfer kinetics. Although the pure AC electrode exhibited a relatively small ΔE_p (110 mV), this value should be interpreted cautiously because its electrochemical response was dominated by capacitive charging rather than a well-defined Faradaic process.

EIS results further supported these observations. Nyquist plots (Fig. 4b) were fitted using the equivalent electrical circuit shown in the inset, incorporating a constant phase element (CPE) to account for the non-ideal capacitive behavior of porous composite electrodes (Gateman et al., 2022). The spectra consisted of a depressed high-frequency semicircle corresponding to the charge-transfer process and an inclined low-frequency region associated with ion diffusion within the porous electrode structure. Gradual decrease in semicircle diameter with increasing AC content indicates a substantial reduction in charge-transfer resistance (R_{ct}). Accordingly, R_{ct} decreased from 148.52 $\Omega \cdot cm^2$ for pristine g-C_3N_4 to 84.56 $\Omega \cdot cm^2$, 46.40 $\Omega \cdot cm^2$, and finally 7.18 $\Omega \cdot cm^2$ for the gCN:AC 25:75 electrode. Interestingly, this value is even lower than that of the pure AC electrode (16.93 $\Omega \cdot cm^2$), demonstrating that the superior electrochemical performance cannot be attributed solely to the intrinsic conductivity of AC but rather to the synergistic interaction between both components. Similar reductions in R_{ct} after incorporation of g-C_3N_4 into conductive carbon matrices have been reported previously (Umapathi et al., 2022). Bode phase plots (Fig. 4c) further confirmed the improved charge-transfer characteristics. The maximum phase angle gradually decreased with increasing AC fraction, indicating faster electrochemical relaxation and a progressively more resistive response. Consistently, impedance magnitude plots (Fig. 4d) revealed continuous decrease in low-frequency impedance with increasing AC content, whereas all electrodes converged to similar impedance values above approximately 1 kHz, confirming comparable solution resistance. These results indicate that the observed differences originate primarily from the electrode/electrolyte interface rather than from the electrolyte itself. In addition to R_{ct}, the CPE exponent (n) was evaluated as an independent EIS-derived indicator of the electrodes' microstructural evolution (Tab. 2). The fitted CPE exponent (n) decreased progressively from 0.955 for pristine gCN to 0.941, 0.867, and 0.778 for the gCN:AC 75:25, 50:50, and 25:75 compositions, respectively, before increasing slightly to 0.790 for the pure AC electrode. Since n reflects the degree of deviation from ideal capacitive behavior and is commonly associated with surface roughness and porosity, this trend provides quantitative support for the increasing real surface area and heterogeneity with AC content inferred from SEM (Fig. 3). The slightly higher n observed for the pure AC electrode relative to the 25:75 composite may reflect a more uniform, self-similar pore structure within the single-component AC film, in contrast to the additional surface heterogeneity introduced by combining two morphologically distinct particle types (gCN nanosheets and porous AC particles) in the composite.

Overall, the electrochemical behavior correlates well with the microstructural evolution observed by SEM. Pure AC electrodes consisted of relatively large particles with incomplete interparticle contacts, whereas incorporation of nanosized gCN filled the interparticle voids and produced a denser, more homogeneous composite structure. Although gCN is intrinsically less conductive than AC, its nanoscale dimensions improve particle packing and increase the effective contact area between adjacent AC particles, thereby reducing contact resistance and facilitating charge transport through the conductive carbon network. Consequently, the gCN:AC 25:75 electrode exhibited the lowest charge-transfer resistance and the fastest electron-transfer kinetics among all investigated compositions. The results demonstrate complementary roles of the two components: gCN contributes electrochemically active surface sites that enhance the Faradaic response, while AC forms the primary conductive network enabling efficient electron transport. It should be noted that the decrease in I_p with increasing AC content and the concurrent decrease in ΔE_p and R_{ct} are not contradictory but reflect two distinct aspects of the electrode/electrolyte interface. ΔE_p and R_{ct} primarily report the facility of interfacial electron transfer and the total real (capacitive + Faradaic) contact area of the composite, both of which improve with AC content due to the higher electrical conductivity, higher specific surface area, and denser particle packing. In contrast, I_p additionally

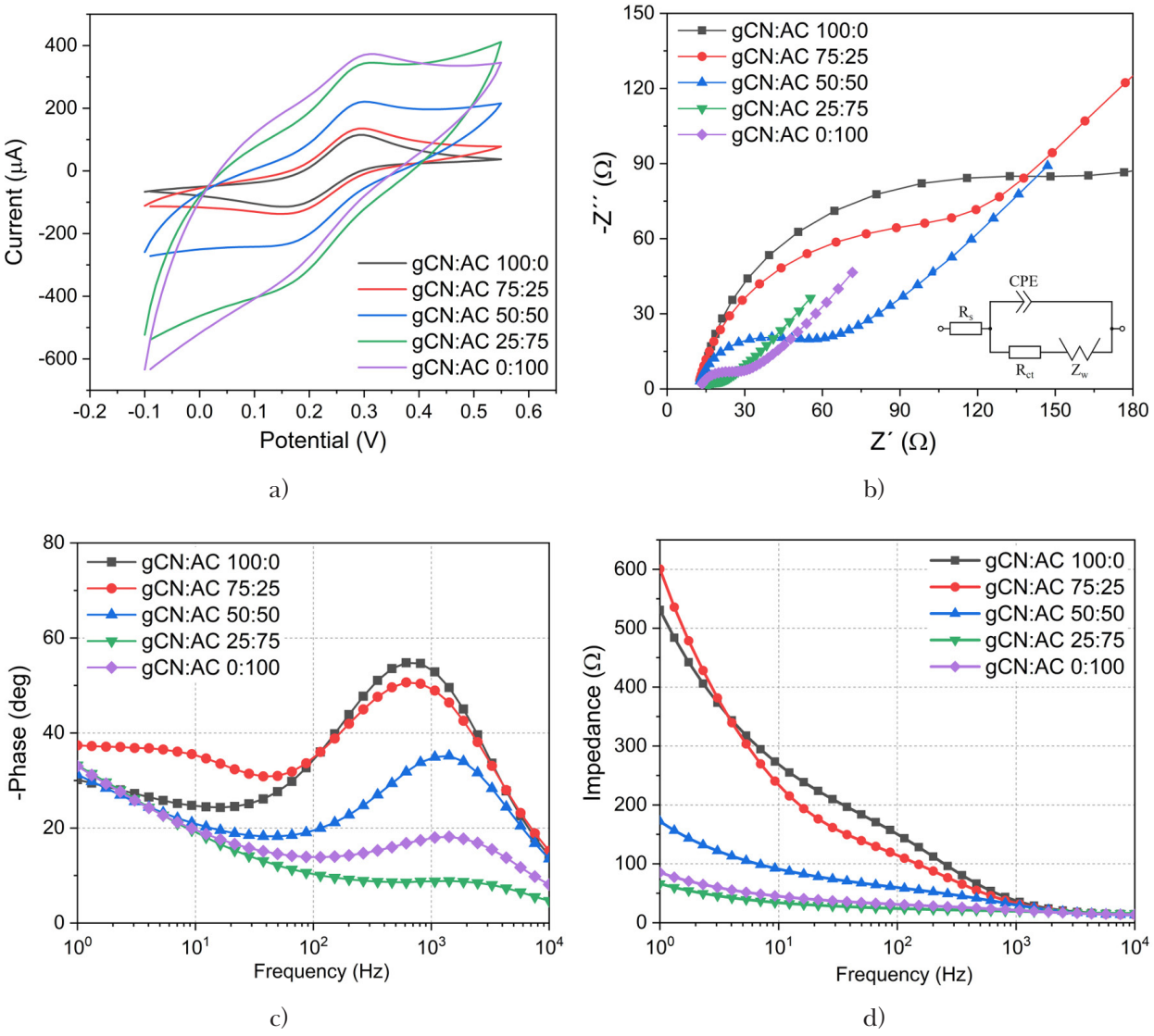


Fig. 4. Electrochemical measurements of screen-printed gCN:AC electrodes. a) Cyclic voltammograms at the scan rate of 100 mV · s^{-1}. Electrochemical impedance spectroscopy measurements: b) Nyquist plots with inserted fitting equivalent circuit, c) Bode phase plots, d) Impedance plots. All electrochemical measurements were performed in an aqueous electrolyte containing 1 mM $[Fe(CN)_6]^{3-/4-}$ and 0.1 M KCl as the supporting electrolyte.

Tab. 2. Electrochemical parameters obtained from CV and EIS measurements of screen-printed gCN:AC electrodes.

Sample gCN:AC	I_{pa} (μA)	*RSD* (%)	I_{pc} (μA)	*RSD* (%)	I_{pa}/I_{pc}	E_{pa} (V)	E_{pc} (V)	ΔE_p (V)	R_{ct} (Ω · cm^2)	*RSD* (%)	*n*
100:0	129.10 ± 2.87	2.22	−120.30 ± 3.30	2.74	−1.07	0.290	0.160	0.130	148.52 ± 8.77	5.90	0.955
75:25	105.90 ± 8.42	7.95	−100.30 ± 7.26	7.24	−1.06	0.290	0.170	0.120	84.56 ± 6.52	7.71	0.941
50:50	88.71 ± 5.66	6.38	−74.60 ± 2.62	3.51	−1.19	0.280	0.180	0.100	46.40 ± 4.13	8.90	0.867
25:75	63.62 ± 3.09	4.86	−53.91 ± 3.40	6.31	−1.18	0.280	0.180	0.100	7.18 ± 1.03	14.35	0.778
0:100	17.20 ± 2.45	14.42	−87.09 ± 7.13	8.19	−0.20	0.270	0.160	0.110	16.93 ± 2.20	12.99	0.790

depends on the density of sites capable of undergoing Faradaic exchange with $[Fe(CN)_6]^{3-/4-}$, which are predominantly associated with gCN rather than AC. As the gCN fraction diminishes, this site density and hence I_p decreases, even as the total electroactive interfacial area and the associated charge-transfer resistance improve. The gCN:AC 25:75 composite therefore combines the most facile

interfacial charge-transfer characteristics with a reduced total Faradaic current, consistent with the complementary and spatially distinct roles of gCN (Faradaic activity) and AC (conductive network/capacitive area) described above. However, it should be taken into consideration that the pronounced capacitive background observed at higher AC content, while not limiting the millimolar-level redox-probe measurements performed in this study, carries important implications for the intended trace-level sensing application. This behavior is well documented for activated carbon, which is known to exhibit large capacitive currents owing to its high specific surface area and porosity, and is therefore not unique to the present composite system. Because the capacitive current is largely independent of analyte concentration (given the large excess of supporting electrolyte used, which fixes the double-layer structure), whereas the Faradaic peak current scales with it, a large and composition-dependent capacitive background is expected to substantially degrade the signal-to-noise ratio and the achievable limit of detection when quantifying analytes at trace concentrations, as would typically be required in practical sensing applications. For practical trace-analyte sensing, additional electrode activation could be beneficial. The choice of an optimal gCN:AC composition may therefore be application-dependent.

Conclusions

This work demonstrates that direct incorporation of graphitic carbon nitride (g-C_3N_4) into activated carbon (AC)-based conductive inks represents a promising strategy for tailoring both the processing characteristics of screen-printing inks and the electrochemical performance of printed electrodes. By systematically investigating the influence of the g-C_3N_4 ratio on rheological, microstructural, and electrochemical properties, this study provides a comprehensive understanding of the interplay between filler composition, printability, electrode architecture, and charge-transfer behavior, offering useful guidelines for the rational design of printable materials for electrochemical sensing applications. All gCN:AC inks exhibited the shear-thinning behavior required for screen printing, while increasing the g-C_3N_4 content markedly increased the low-shear viscosity and promoted rapid structural recovery after shear. The observed viscosity overshoot indicates that g-C_3N_4 plays a dominant role in reconstructing the internal particle network after deformation, contributing to improved dimensional stability of the printed patterns. It should also be acknowledged that the non-conductive ethyl cellulose binder used to formulate printable inks may partially restrict access to electroactive sites on both gCN and AC particles. Its quantitative contribution to the electrochemical response was not isolated in the present study and requires further investigation, for example, through systematic variation of binder content or comparison with binder-free or conductive-binder electrode formulations. SEM measurements showed that the combination of nanosized gCN with micrometer-sized AC produces a hierarchical composite structure. The g-C_3N_4 particles efficiently fill the interparticle voids between larger AC particles, resulting in denser packing and improved structural homogeneity compared with electrodes containing only AC. Although g-C_3N_4-containing electrodes exhibited drying-induced microcracks, the composite architecture maintained excellent adhesion to the FTO substrate and promoted improved particle-to-particle contact. Electrochemical measurements revealed complementary roles of both components. While both g-C_3N_4 and AC contributed to the Faradaic response, g-C_3N_4 provided abundant electrochemically active surface sites, whereas AC primarily established an efficient conductive network that substantially reduced the charge-transfer resistance. Among the investigated electrodes, the gCN:AC 25:75 composite exhibited the most favorable overall electrochemical performance, combining the lowest charge-transfer resistance with the smallest peak-to-peak separation, which indicates the most facile interfacial electron-transfer kinetics, despite a lower total Faradaic peak current arising from the reduced density of g-C_3N_4-associated active sites at this composition. These improvements originate from the synergistic interaction between both materials rather than from the individual properties of either component alone. The proposed gCN:AC composite inks represent a promising material platform for screen-printed electrochemical sensors. The ability to tune their rheological and electrochemical properties through filler composition may support the development of printed sensors with improved analytical performance. It should be noted that the pronounced capacitive background associated with higher AC content carries important implications for trace-level sensing applications, where it is expected to degrade the signal-to-noise ratio and limit of detection. The choice of an optimal gCN:AC composition may therefore be application-dependent with additional electrode activation recommended where minimizing background is prioritized over interfacial charge-transfer kinetics.

Acknowledgement

This work was supported by the EU Next Generation EU through the Recovery and Resilience Plan for Slovakia under the project No. 09I05-03-V02-00037 (2DSuperCap).

References

Alwin E, Kočí K, Wojcieszak R, Zielinski M, Edelmannová M, Pietrowski M (2020) Materials 13: 2756.

Mutic S, Durdic S, Petrovic S, Gemeiner P, Stankovic D, Anojčic J (2024) Electrochim. Acta 500: 144755.

Budny F, Jarczewska M, Walter PA, Lepak-Kuc S, Baraniecki D, Peplowski A, Jakubowska M (2022) Eng. Proc. 21(1): 3.

Crapnell RD, Banks CE (2024) ChemElectroChem 11: e202400370.

de Faria L, Villafuerte LM, do Nascimento SFL, de Sá IC, Peixoto DA, de Ribeiro RS, Nossol E, de Lima T, Semaan FS, Pacheco WG, Dornellas RM (2024) Food Chem. 442: 138497.

Gateman SM, Gharbi O, de Melo HG, Ngo K, Turmine M, Vivier V (2022) Curr. Opin. Electrochem. 36: 101133.

Gemeiner P, Mikula M (2013) Acta Chim. Slov. 6: 29—34.

Gibi Ch, Liu CH, Barton SC, Anandan S, Wu JJ (2024) J. Taiwan Inst. Chem. E. 154: 105071.

Gissawong N, Srijaranai S, Boonchiangma S, Uppachai P, Seehamart K, Jantrasee S, Moore E, Mukdasai S (2021) Microchim. Acta 188: 208.

Hatala M, Gemeiner P, Hvojnik M, Mikula M (2019) J. Mater. Sci.: Mater. Electron. 30: 1034—1044.

Jahani PM, Aflatoonian MR, Rayeni RA, Di Bartolomeo A, Mohammadi SZ (2022) Food Chem. Toxicol. 163: 112962.

Li J, Shen B, Hong Z, Lin B, Gao B, Chen Y (2012) Chem. Commun. 48 (98): 12017—12019.

Orzari LO, Kalinke C, Silva-Neto HA, Rocha DS, Camargo JR, Coltro WKT, Janegitz BC (2025) Anal. Chem. 97: 1482—1494.

Puentes-Prado E, Gutiérrez-Granados S, Gomez-Solís C, Ramírez-García G (2022) FlatChem 35: 100412.

Santos AM, Silva TO, Feitosa MHA, Oliveira IGS, Wong A, Souto RS, Moraes FC, Ruotolo LAM, Barros WRP, Lanza MRV (2025) Talanta 285: 127412.

Singh AK, Agrahari S, Gautam RK, Tiwari I (2024) Environ. Sci. Pollut. Res. 31: 67339—67354.

Umapathi R, Raju ChV, Ghoreishian SM, Rani GM, Kumar K, Oh MH, Park JP, Huh YS (2022) Coord. Chem. Rev. 470: 214708.

Wang H, Xie A, Li S, Wang J, Chen K, Su Z, Song N, Luo S (2022) Anal. Chim. Acta 1211: 339907.

Weldon AL, Joshi K, Routh AF, Gilchrist JF (2017) J. Colloid Interface Sci. 487: 80—87.

Zhang X, Zhang XR, Yang P, Chen HS, Jiang SP (2022) Chem. Eng. J. 450: 138030.